

SPECTRAL STRUCTURE IN FR II RADIO GALAXIES AND JETS

KARI TREICHEL AND L. RUDNICK

Department of Astronomy, University of Minnesota, 116 Church Street SE, Minneapolis, MN 55455; kari@astro.umn.edu, larry@astro.umn.edu

M. J. HARDCASTLE

H. H. Wills Physics Laboratory, University of Bristol, Royal Fort, Tyndall Avenue, Bristol BS8 1TL, UK; M.Hardcastle@bristol.ac.uk

AND

J. P. LEAHY

Jodrell Bank Observatory, University of Manchester, Macclesfield, Cheshire SK11 9DL, UK; jpl@jb.man.ac.uk

Received 1999 March 17; accepted 2001 July 11

ABSTRACT

Using spectral tomography to separate overlapping spectral features in a sample of FR II radio galaxies, we find a variety of spatial/spectral features that are not easily described in the context of current models. In particular, we find mixtures of flat- and steep-spectrum features in the hot spot regions and nonmonotonic spectral index gradients along jets. Additional findings include spectral gradients in compact hot spots and possible transitions in jet properties at the downstream ends of the diffuse lobes. The complexity of behaviors uncovered here points to the need for a thorough investigation of numerical models for radio galaxies, as well as for detailed observational studies of larger, unbiased samples. We also perform the first quantitative assessment of errors in the use of spectral tomography for spectral index measurements.

Subject headings: galaxies: individual (3C 401, 3C 438) — galaxies: jets — galaxies: structure — radiation mechanisms: nonthermal — radio continuum: galaxies

1. INTRODUCTION

Radio source spectral indices are used to probe the gain and loss mechanisms of the relativistic electron population in extragalactic radio sources. Steeper spectra may indicate that the electrons in the source have “aged” through synchrotron and other losses. Flatter spectra can be caused by in situ particle acceleration or compression of the medium. (Leahy 1991; Eilek & Hughes 1991). The spectral index variations in a source are therefore fundamental for testing models of the evolution of the relativistic particle populations in radio galaxies. The relative importance of acceleration at the jet terminus, along the jet itself, and in the more diffuse lobes is indeterminate at present. Challenges to the standard picture from recent numerical simulations (see, e.g., Tregillis, Jones, & Ryu 2001) and from nonthermal emission in optical and X-ray bands (see, e.g., Celotti, Ghisellini, & Chiaberge 2001; Wilson, Young, & Shopbell 2001) raise questions about the origins of spectral variations in the much lower energy radio spectra.

Unfortunately, the observation and interpretation of spectral variations in radio galaxies is often ambiguous (see, e.g., Rudnick 2001a). One problem is that the observed spectral index of a feature in a radio source is misleading when two structures with different spectral indices overlap in the plane of the sky. For example, flatter spectrum jets often overlap steeper spectrum lobes. Spectral tomography is one way around this problem: a feature with a specified spectral index can be subtracted out of the image, leaving only the second structure.

Spectral tomography has been used to analyze the spectra of several wide-angle tail sources (WATs; Katz-Stone & Rudnick 1997b; Rudnick & Katz-Stone 1996) and compact steep-spectrum sources (Katz-Stone & Rudnick 1997a). Tomography of one FR II galaxy, Cygnus A, isolated features similar to those seen in the “frequency-corrected” images of this prototypical source (Rudnick,

Katz-Stone, & Anderson 1994). In each case, features not predicted by current radio galaxy models were found. We therefore initiated this exploratory study of additional FR II radio galaxies using existing maps. Below we examine the results from our spectral tomography on these distant FR II sources and estimate the spectral index of several jets along their lengths. We then briefly describe some implications of these results for radio galaxy models and make suggestions for future work.

2. OBSERVATIONS

The maps used in this study were all obtained from previous studies. The maps at 8.4 GHz are VLA¹ data from Hardcastle et al. (1997). The maps of the sources at a second frequency come from Leahy & Perley (1991) for 3C 173.1, 3C 349, 3C 381, and 4C 14.11 (VLA data), from Leahy, Bridle, & Strom (1997)² for 3C 153, 3C 401, and 3C 438 (VLA and MERLIN data),³ and from Laing (1999, private communication) for 3C 132 (VLA data). Table 1 contains a list of each source at both frequencies used and the beam size and noise of each map. For all maps, the center of the u - v plane was well sampled, so the flux in the extended structure was well constrained. Total intensity maps of the two sources with prominent jets, 3C 401 and 3C 438, are shown in Figures 1 and 2. Tests of map fidelity and the robustness of the tomography results are discussed in the next section.

¹ The Very Large Array is a facility of the National Radio Astronomy Observatory, operated by Associated Universities, Inc., under contract with the National Science Foundation.

² Available at <http://www.jb.man.ac.uk/atlas>.

³ MERLIN is a national facility operated by the University of Manchester on behalf of the UK Particle Physics and Astronomy Research Council (PPARC).

TABLE 1

FREQUENCY, RESOLUTION, AND NOISE LEVELS FOR THE SOURCES STUDIED

Source	Frequency (GHz)	Beam Size (arcsec)	rms Noise (μ Jy/beam)	Reference
3C 132.....	4.96	0.33	38	1
	8.44	0.22	29	2
3C 153.....	1.53	0.15	95	3
	8.44	0.25	28	2
3C 173.1.....	1.45	2.60	77	4
	8.44	2.60	89	2
3C 349.....	1.50	2.90	102	4
	8.44	2.90	59	2
3C 381.....	1.45	3.25	151	4
	8.44	3.25	99	2
3C 401.....	1.53	0.35	76	3
	8.44	0.27	24	2
3C 438.....	1.53	0.29	97	3
	8.44	0.23	25	2
4C 14.11.....	1.45	3.00	68	4
	8.44	3.00	29	2

REFERENCES.—(1) Laing, 1999 private communication. (2) Hardcastle et al. 1997. (3) Leahy et al. 1997; available at <http://www.jb.man.ac.uk/atlas>. (4) Leahy & Perley 1991.

3. ANALYSIS AND RESULTS

3.1. Map Preparation

Before constructing the spectral tomography galleries, we first convolved the maps at each frequency to the same resolution. Then the maps were aligned by matching up the peak of the core or a hot spot (if the core was absent from the images). The peak locations were found by fitting the core or hot spot to elliptical Gaussians. These alignments were verified by subtracting the maps at the two frequencies with small relative shifts in position and minimizing the rms residuals in a small area surrounding and including the core or hot spot. Any misalignment would result in a gradient in spectral index seen throughout the spectral tomography maps. No such global gradient was seen, and the alignments are correct to within 0.1 pixels.

3.2. Map Fidelity

Because our work was based on previously published

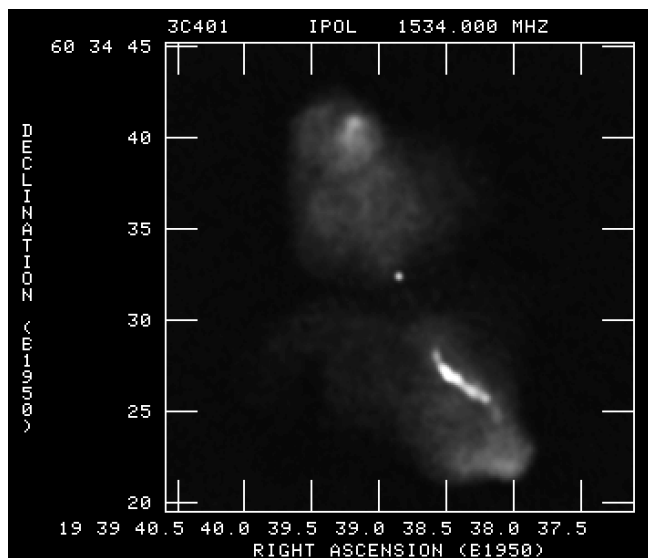


FIG. 1.—Total intensity map of 3C 401 at 1.5 GHz

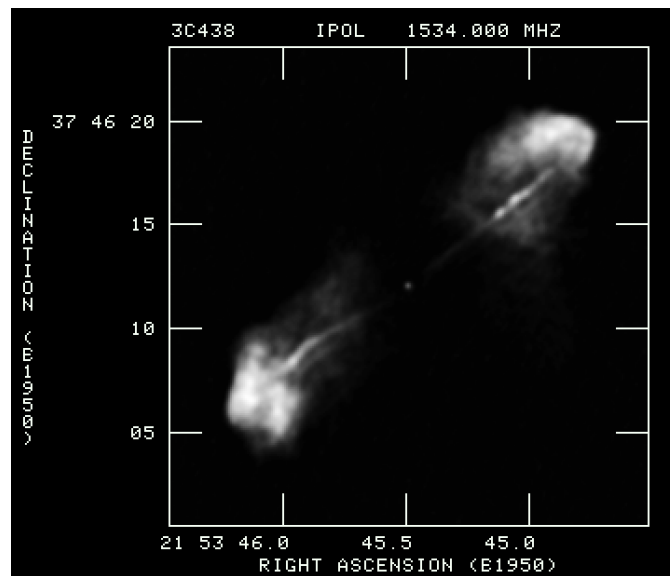


FIG. 2.—Total intensity map of 3C 438 at 1.5 GHz

maps, constructing the spectral tomography galleries involved comparing images that had normally been imaged and deconvolved using different algorithms or weightings. In addition, some of our pairs of maps were made from observations that had very different samplings of the u - v plane. It was important to be certain that these differences did not affect the reliability of the tomography images for the structures of scientific interest.

To assess the effect of these differences, we returned to the original uv data for the two jetted sources, 3C 401 and 3C 438. The 8.4 GHz VLA data for these sources are a combination of observations with the A, B, and C configurations of the VLA, with no more than an hour's observation at each configuration (together with a 10 minute snapshot in the D configuration in the case of 3C 438). At our second frequency, 1.4 GHz, the data consist of a long track with MERLIN, together with short observations with the A configuration of the VLA. While the longest and shortest baselines sampled by these observations are very similar, the detailed coverage of the u - v plane is quite different. Because of the uneven sampling of the u - v plane, the MERLIN-plus-VLA data were particularly prone to the "rice pudding" effect introduced by instabilities in the CLEAN algorithm (Cornwell 1983), and so they were deconvolved using a hybrid CLEAN/MEM technique (see, e.g., Leahy & Perley 1991), whereas the 8.4 GHz VLA data were simply deeply CLEANed. Because of these differences, and because of the complex structure seen in the two sources, they are good test cases for our investigation.

We quantified the effects of different sampling and deconvolution by simulating observations of the *same* source using the two different data sets. To do this we took the CLEAN components from a deep CLEANing of the 8.4 GHz data for the two sources at full resolution, assuming that this map represents adequately the total intensity structures of interest. Using the AIPS task UVSUB, we replaced the real visibilities in both 1.4 and 8.4 GHz UV data sets with a model based on the CLEAN components. We then mapped the data sets, using deconvolution techniques that were similar to those used to produce the real

maps, convolved to a common resolution, and compared the resulting images.

If the deconvolution had been ideal and the sampling perfect, we would expect to obtain identical maps from this process. In fact, there were small differences, particularly in the low surface brightness structure, which presumably result either from different sampling or, more likely, from artifacts introduced by deconvolution (such as rice pudding effects in the deeply CLEANed simulated 8.4 GHz maps). However, there were no *systematic* differences in the sources, which would reflect serious undersampling, and the high surface brightness regions of the simulated sources were essentially identical in the two maps. When we constructed maps of “spectral index” between the two maps, the rms variation was of order 0.05 in the high surface brightness regions, and the mean was indistinguishable from zero. We are therefore able to conclude that the differences in u - v -plane sampling and deconvolution do not introduce any significant errors into the analysis that follows; by contrast, the *detailed* structure of low surface brightness tomography images is not reliable and not discussed here.

The deconvolution procedures recovered most of the expected total fluxes. The maps contain approximately 90% and 100% at 1.4 and 8.4 GHz, respectively, for 3C 401 and 95% and 100% for 3C 438. Any missing fluxes, which are likely to correspond to the largest-scale components, would not significantly affect any of the results in this paper. Tomography of well-sampled small-scale features, as discussed below, effectively removes any biases due to underlying diffuse structures, so errors in the reconstruction of the latter do not propagate. This would not be true, by contrast, with the standard method of calculating spectral indices using map division.

3.3. Spectral Tomography

To take a closer look at overlapping structures, one wants to first subtract out of the image a feature of a particular spectral index. Because we do not know a priori which spectral index to use to remove confusing structures, we construct a gallery of maps, each with a different spectral index zeroed out. That is, we construct a set of maps M_{α_t} , where

$$M_{\alpha_t} = M_{\nu_1} - M_{\nu_2} \exp [\alpha_t \ln (\nu_1/\nu_2)] .$$

If a structure has spectral index α_t , it will disappear in map M_{α_t} .

The intensity of the signal that is left behind in a tomography image has two origins: its overall intensity and a factor that depends on the difference between its actual spectral index and α_t . We quantify this as follows. Suppose a feature has intensities A_{ν_1} and A_{ν_2} and a spectral index α_0 that is different from that of a particular tomography image M_{α_t} . Then its intensity A_t in that tomography image will become

$$A_t = A_{\nu_2} - \left(\frac{\nu_2}{\nu_1}\right)^{\alpha_t} A_{\nu_1} = S_{\nu_1} \left(\frac{\nu_2}{\nu_1}\right)^{\alpha_0} \left[\left(\frac{\nu_2}{\nu_1}\right)^{(\alpha_t - \alpha_0)} - 1 \right] .$$

Thus, the presence of a feature in a tomography image shows that it has a different spectral index than the corresponding α_t . However, its strength is the product of both its original intensity and a function depending on the differ-

ence between α_t and α_0 . One cannot deduce the spectral index of a feature from tomography images, *except where it disappears*.

Because spectral tomography maps are a linear combination of total intensity maps, they have the same reliability and noise characteristics as the original intensity maps. Therefore, in the absence of deconvolution or other systematic problems, the off-source noise can be used as an indicator of the reliability of individual features on the tomography map. Deconvolution problems, such as those described above, can be present in the same way on intensity or tomography maps. However, such problems are often more visible on tomography images; this is because a large fraction of the signal has been subtracted, while the artifacts at the two frequencies are unlikely to be identical and therefore do not subtract cleanly. We will refer back to these guidelines in our discussion of findings from the tomography images.

3.3.1. Mixed Spectral Indices in 3C 401 and 3C 438

When looking through the galleries, the first thing one notes is the mixture of spectral indices throughout the lobes of the sources. The most dramatic example is in source 3C 438, as shown in Figure 3. Figure 3 shows two spectral tomography maps, the north lobe of 3C 438, at $\alpha_t = 0.81$, and the south lobe, at $\alpha_t = 1.02$. In these maps, lighter tones indicate regions with spectral index flatter than the respective above values of α_t , while dark regions have an index steeper than α_t . For example, the jet is flatter than α_t in both these maps and shows up white. In the southern lobe, one can see a dark ring that has a steeper spectral index. There is also a light, therefore flat, C-shaped structure to the west.

Regarding the reliability of features, the off-source ripple indicates the level of background noise. Additional spurious details are seen in the lobe emission, likely from CLEAN artifacts, which can be recognized and assessed as they would in any other total intensity image. The existence of the separate flat/white and steep/black features is a clear, high signal-to-noise-ratio result. The detailed small-scale fluctuations in the lobes are not. A slice along the northern jet from the Figure 3 tomography image is shown in Figure 4 and details the noise trustworthiness of the various features.

3C 401 and 3C 153 have complex spectral structures similar to those in 3C 438. The other sources have spectral gradients in their hot spots (see below) but lack sufficient resolution or dynamic range to show more than an overall steepening of the lobe going from the hot spots toward the core.

When examining the spectral tomography maps, we noted that the hot spots seemed to have a spectral index gradient, with α being about 0.2 flatter at the outer edges of the hot spots than at the inner edges. The first assumption, upon seeing this, was that the maps were misaligned, because a spectral index gradient can be a product of misalignment. But if the maps were misaligned, the gradient would be in the same direction in both hot spots, not in opposite directions, as we see in Figure 5. In this image of a slice across a tomography map $M_{0.78}$, intensities less than zero indicate regions with $\alpha < 0.78$ and intensities greater than zero indicate $\alpha > 0.78$. Of the eight sources we studied, four had no well-defined hot spots or confusing structures near the hot spots. In the remaining four sources with clear hot spots, we saw a spectral index gradient clearly in three

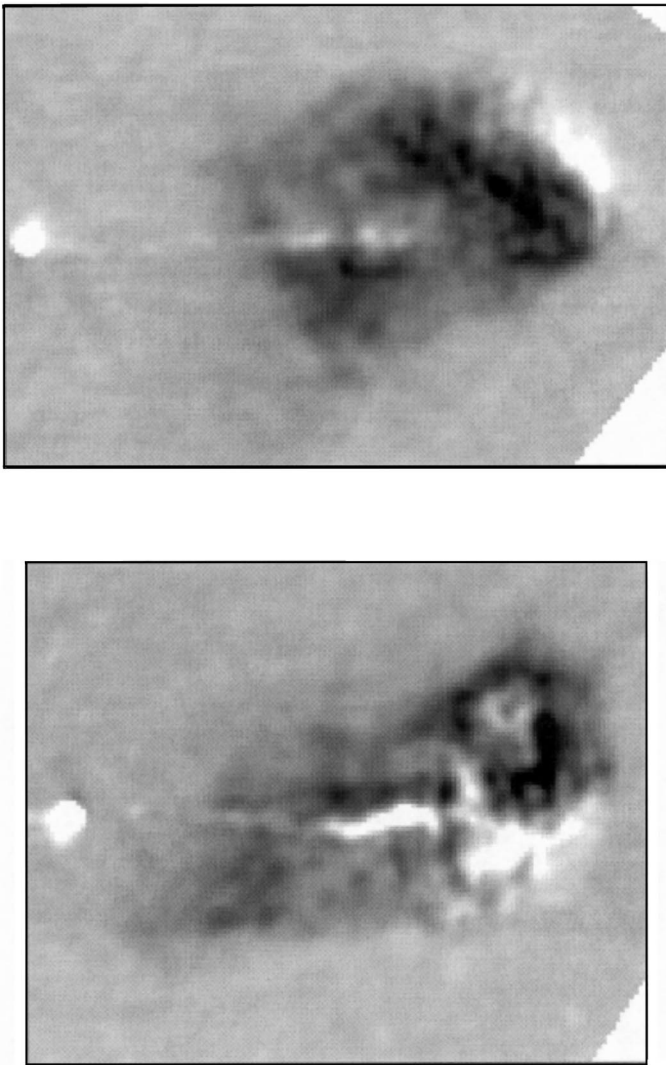


FIG. 3.—Spectral tomography maps of 3C 438, showing the mixture of steep and flat spectral indices in each lobe. The units of these maps are janskys per beam, as in the original intensity maps. The off-source gray regions have means near zero and fluctuations that give an indication of the noise. Lighter regions are those flatter than $\alpha = 0.81$ and 1.02 for the top and bottom, respectively. Darker regions are steeper than these respective values. Fine-scale mottling in the steep regions is an artifact of the X-band map reconstruction.

sources (3C 132, 3C 349, and 3C 381) and tentatively in the fourth (3C 173).

3.3.2. Structure Parallel to Jet

Among these structures of differing spectral index, one can see a structure that runs parallel to the jet in 3C 438. This structure has a steeper spectral index ($\alpha = 1.2$) than the jet, as is shown in Figure 6.

To take a closer look at this structure, we compressed the approximately $4''$ in the northern lobe that included the parallel structure to create an integrated slice across the jet. This integrated slice is shown in Figure 7 for 8.4 GHz, 1.5 GHz, and $M_{0.6}$, where the jet has disappeared from the tomography maps. The parallel structure is easily seen in the 1.5 GHz map but is weaker in the 8.4 GHz map. The slices show that there may also be a steep-spectrum feature partly blended with the jet on the side opposite the parallel structure.

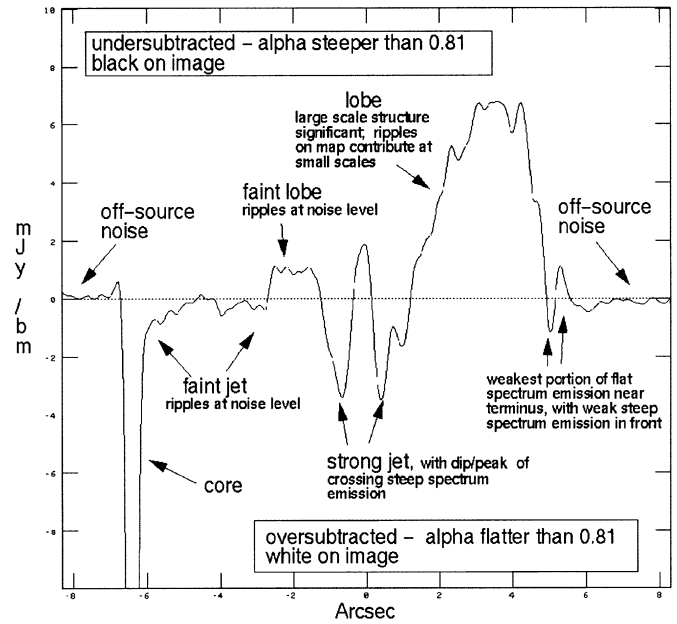


FIG. 4.—Slice along the northern jet of 3C 401 from the $\alpha = 0.81$ tomography image (Fig. 3, top), commenting on the reliability of various features.

Figure 7 clearly shows that the structure we examined consists of a single peak, not multiple peaks or a sinusoidal pattern, which would be expected if the structure were simply an imaging artifact. To further ensure that the struc-

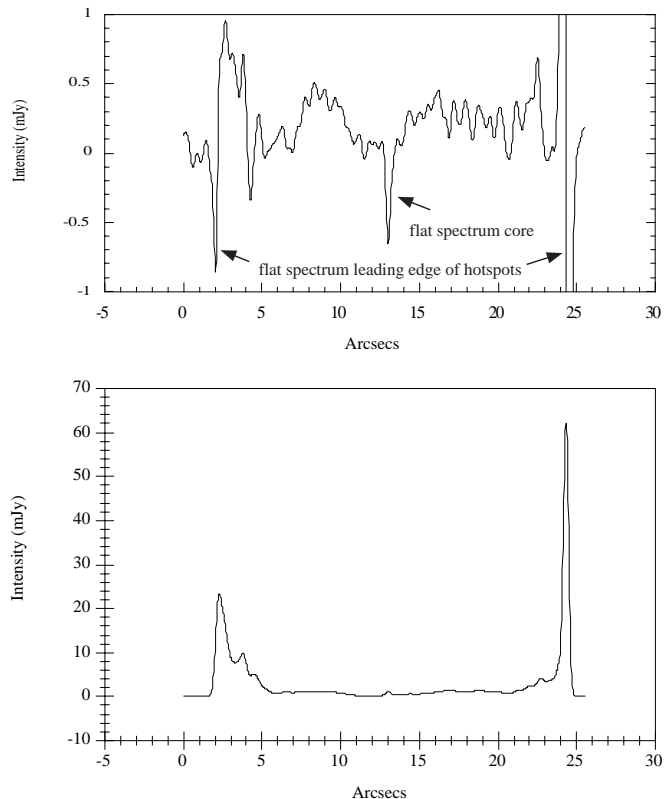


FIG. 5.—Spectral tomography slice (top) and total intensity of a slice (bottom) along the length of 3C 132 from hot spot to hot spot.

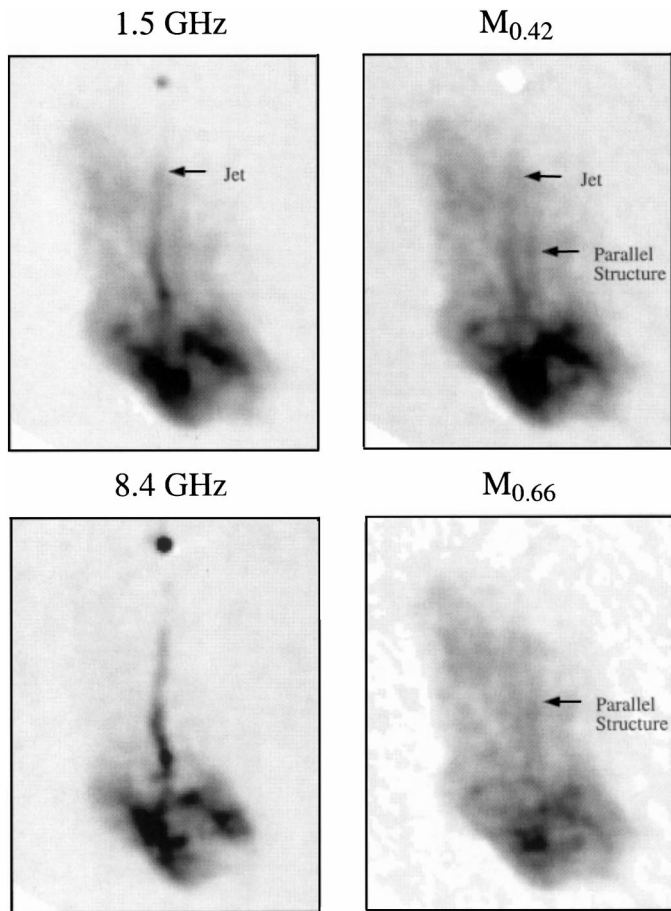


FIG. 6.—Gray-scale total intensity images and spectral tomography maps of the south lobe of 3C 438, showing the structure running parallel to the jet.

ture was not an imaging artifact, slices were taken along the jet and along the parallel structure. These slices are shown in Figure 8. The intensity of the parallel structure does not mimic the major small-scale peaks in the jet, as would be expected for an imaging artifact. Furthermore, a similar structure parallel to the jet can be seen in the southern lobe, where the jet bends. In the southern lobe, the parallel structure closely, but not perfectly, follows that bend of the jet. This behavior is not likely to result from an imaging artifact.

3.4. Error Analysis of Jet Spectra

To obtain more quantitative results on jet spectra in the two strongly jetted sources, 3C 401 and 3C 438, slices were taken across the jet for each spectral index α_t in the gallery. When $\alpha_t = \alpha_{jet}$, the jet will disappear from the slice. Note, however, that the intensity at the position of the jet in M_{α_t} does not go to zero, but instead reflects the residual lobe intensity at α_t .

Determining α_{jet} , when the jet disappears, is necessarily subjective. In some cases, the determination is straightforward; in others, confusion from the background (lobe) emission makes identification of the local jet spectral index difficult. Examples of both these cases are shown in Figure 9. Below, we estimate the errors in our results caused by confusing structures.

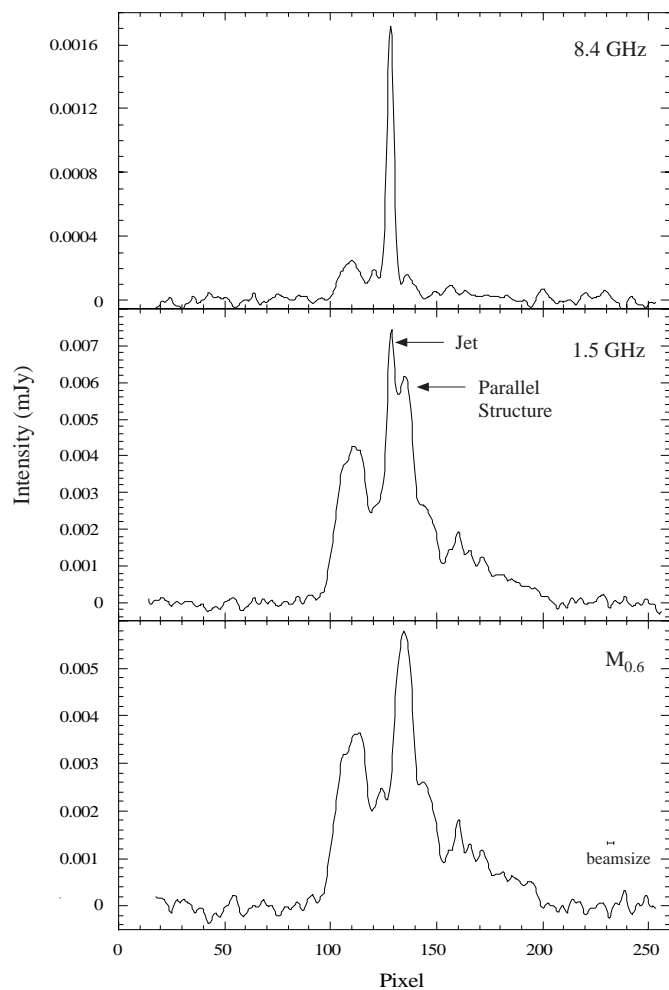


FIG. 7.—Integrated slices across the northern jet of 3C 438, showing the parallel structure.

To test the reliability of determining spectral indices using tomography in the presence of confusing structures, we made a series of simple, one-dimensional, numerical models at two frequencies with a ratio of 1.44:1. These

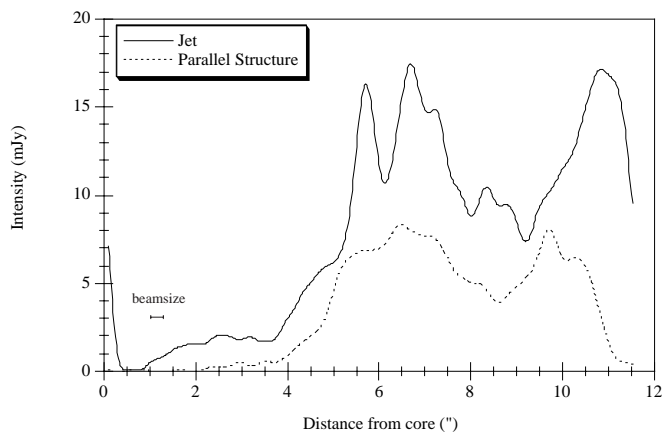


FIG. 8.—Slices along the jet and parallel structure in 3C 438 at 1.5 GHz, showing similar but not identical behavior. The rms noise for this image is $97 \mu\text{Jy}$.

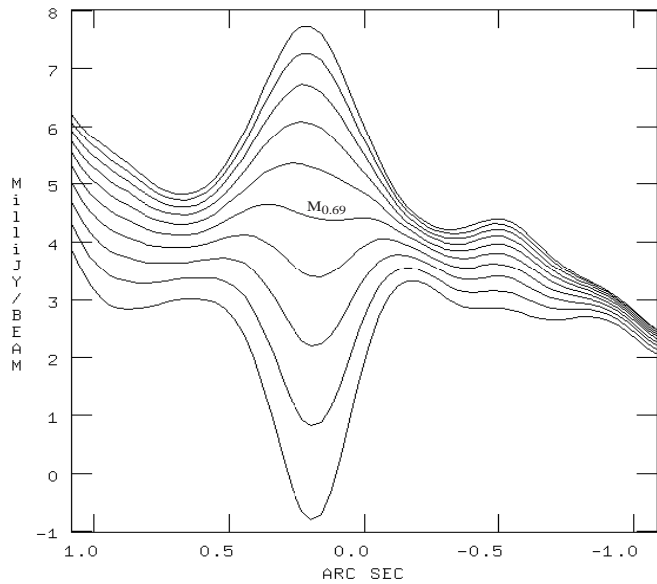


FIG. 9a

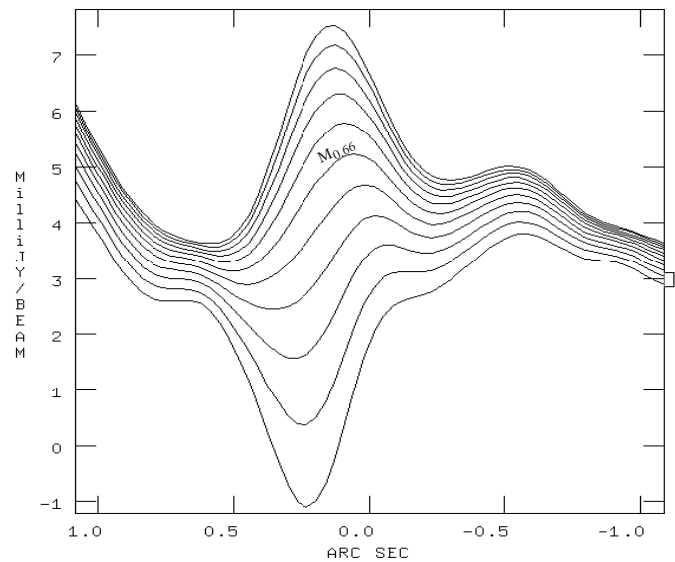


FIG. 9b

FIG. 9.—(a) Series of slices through the jet spectral tomography images for a range of spectral indices. The labeled slice indicates the one identified by eye as corresponding to the jet spectral index. (b) Same as (a), but showing greater confusion from the noise and extended structure.

models included a narrow Gaussian jet (FWHM = 3), a wide Gaussian lobe (FWHM = 20), and superposed sine waves of different wavelengths to simulate irregularities in the lobe emission. The spectral index of the jet was set to 0.5, while those of the lobe and irregularities were set to 1.1 (see Fig. 10). Then we varied several characteristics of the jet and lobe, including the position of the jet relative to the lobe and the width, intensity, and phase of the sine wave. Obviously, using a sine wave to simulate random irregularities is artificial, because the eye can detect the sine wave pattern in the unconfused area and follow it into the confused area, i.e., the jet. On the other hand, when looking at the real data, it is impossible to tell when a confusing structure is perfectly overlapping the jet. But using the sine wave yields a useful approximation of the errors in identifying the “correct” jet spectral index.

The most important criteria for whether the correct spectral index was determined were the interfering sine wave’s width and intensity at the jet position (i.e., the phase of the sine wave); the jet’s position with respect to the lobe was not important. In an examination of the slices, any sine waves significantly wider than the jet were easily distinguishable; determining the spectral index of the jet was difficult only when the width of the sine wave was on the same order as that of the jet. Figure 11 shows how the width of the sine wave affects the size of the error in α . Plotted in this figure are the differences between the correct α and the α determined by spectral tomography for sine waves of different wavelengths and different offsets of the peak from the jet. This figure shows that the correct spectral index falls within the range mean \pm error about two-thirds of the time, with errors calculated analytically as discussed below. This implies that our calculated errors correspond to 1σ .

Figure 12 shows an extreme case, where the minimum of the sine wave occurs at the jet. In this situation, inspection by eye yielded a spectral index that was incorrect by 0.21. Analytically, the same error can be found by defining the true spectral index as $\alpha_0 = \ln(I_1/I_2)/\ln(v_1/v_2)$, where I_1 and

I_2 are the intensities at frequencies ν_1 and ν_2 , respectively. With a confusing structure of intensity b_1 and b_2 , the observed spectral index will be $\alpha_{\text{obs}} = \ln[(I_1 + b_1)/(I_2 + b_2)]/\ln(\nu_1/\nu_2)$. This leads to an error in spectral index of the jet of

$$\begin{aligned} \delta\alpha &= \alpha_{\text{obs}} - \alpha_0 = \frac{\ln[(I_1 + b_1)/(I_2 + b_2)] - \ln(I_1/I_2)}{\ln(\nu_1/\nu_2)} \\ &= \left[\ln\left(\frac{I_1 + b_1}{I_1}\right) - \ln\left(\frac{I_2 + b_2}{I_2}\right) \right] / \ln\left(\frac{\nu_1}{\nu_2}\right). \end{aligned}$$

We thus took the above analytical errors as a reasonable estimate and applied them to the real sources. Using slices from the total intensity maps at both frequencies, the intensities of the jet (I_1 and I_2) and irregularities in the lobe (b_1 and b_2) were estimated by eye. Because our models showed that irregularities with a width up to twice that of the jet created the largest errors, any irregularities on scales larger than this were ignored. To be conservative, we chose values for b_1 and b_2 equal to the largest deviations from the smoother background lobe. See Figure 13 for an example of how these values were determined. In this slice, the lobe intensity is estimated to be ≈ 4.5 mJy beam $^{-1}$. This yields a conservative estimate for the jet intensity of ≈ 2.0 mJy beam $^{-1}$. The intensity of the “noise” that we modeled as a sine wave is estimated as half the total peak-to-peak deviation from the lobe—in this case ≈ 0.8 mJy beam $^{-1}$.

In one situation, the spectral index of the jet could not be determined because of a third structure overlapping both the jet and lobe. This occurred in the northern lobe of 3C 438, where a ring crosses the jet about 5" from the core.

Rudnick (2001b) also determined the spectral index along the jets of 3C 438 and 3C 401, using a multiresolution filtering technique that automatically removes the contributions from large-scale structures. The spectral index values found in that independent method agree quite well with those found here using spectral tomography.

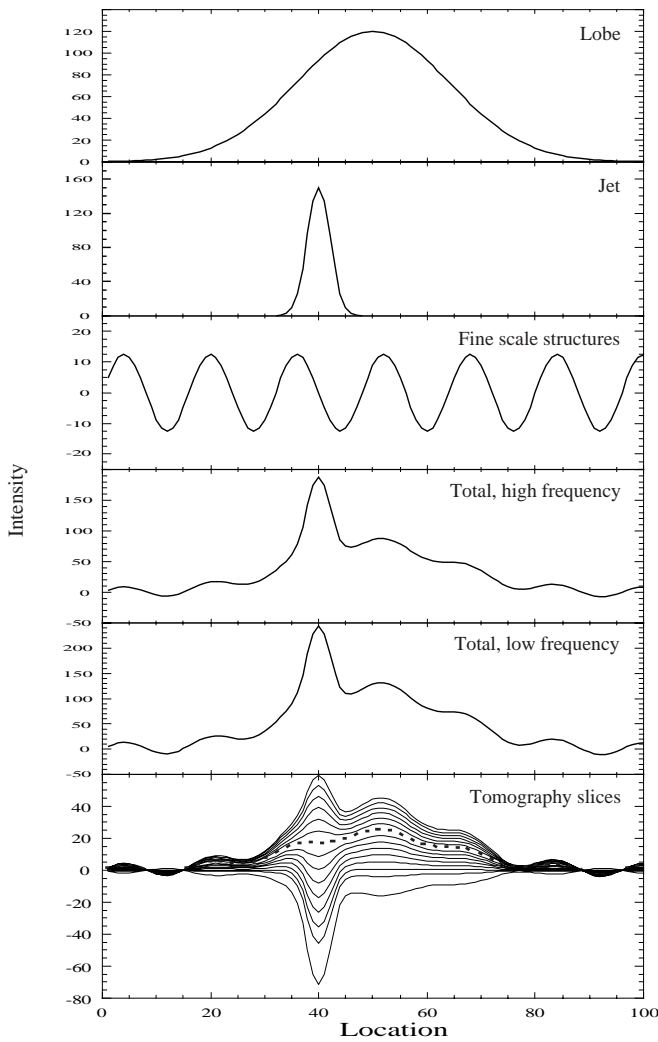


FIG. 10.—Example of the models used to estimate the errors in spectral tomography determinations of spectral index. Top three panels show the individual components. The next two panels show the sum of the components, weighted by spectral index at both high and low frequencies. The bottom panel shows slices through the tomography maps of different spectral indices. The dashed line is the slice corresponding to the correct spectral index of the jet and is also the slice we picked as the correct one.

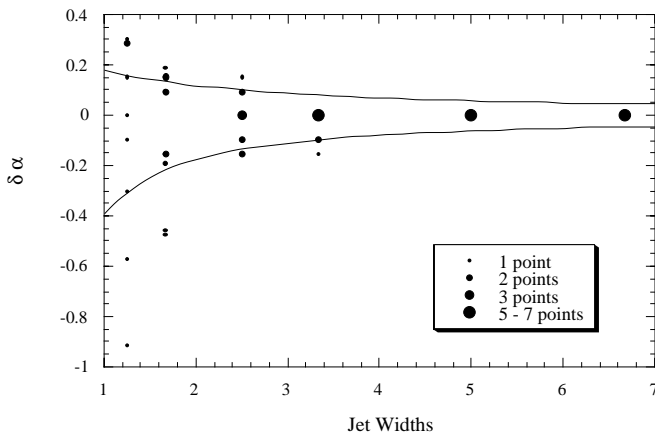


FIG. 11.—Error in α from tomography of model jets vs. wavelength of the sine wave used to simulate noise. The closer the width of the sine wave is to the width of the jet, the larger the errors in α . The lines are the analytical errors found using the equation in text, where b_1 was taken as a sine wave. The size of the symbols indicates the number of times the error in spectral index took on that value.

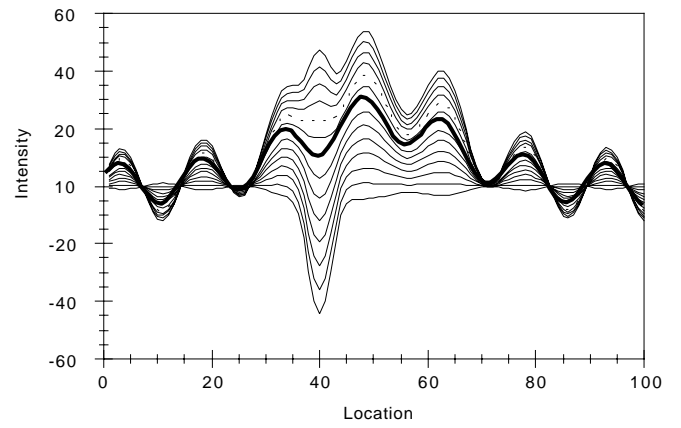


FIG. 12.—Spectral tomography slices of a model with significant confusion from the sine wave “noise.” *Thick line*: Slice corresponding to the correct spectral index ($\alpha = 0.5$); *dashed line*: slice identified by tomography ($\alpha = 0.71$).

3.5. Jet Properties

In order to compare the jet spectra with other jet properties, we determined the FWHM and peak intensity of the jet and the peak intensity of the lobe by fitting a narrow and a wider Gaussian to a slice perpendicular to the jet at each location. Occasionally, a third, narrow Gaussian was used to improve the fit when a filament or other structure was present in the slice. The errors shown for the width and intensity of the Gaussians are formal errors in the fit. They do not take into account the fact that the jet and lobe are not perfect Gaussians and that intermediate-size structures may also be present.

Figure 14 shows the results for 3C 401. In this jet, the spectral index stays nearly constant at $\alpha = 0.54$ along the length of the jet. The jet width is unresolved by the X-band $0''.27$ beam until $\approx 7''$ from the core. Figures 15 and 16 are

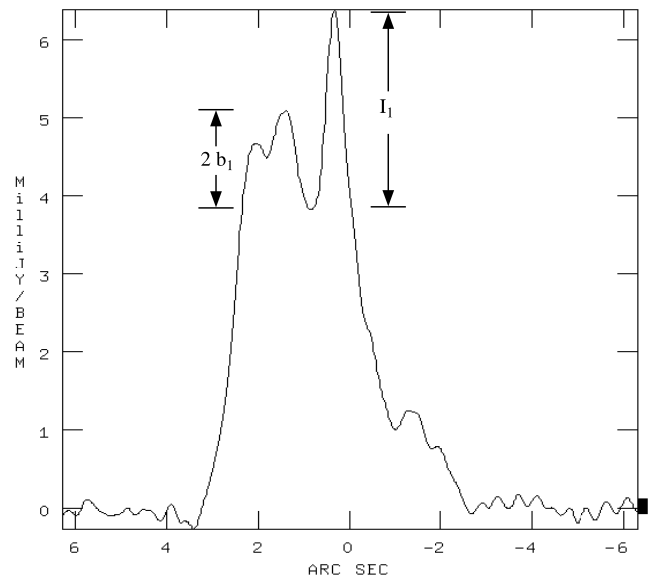


FIG. 13.—Example of determining I_1 and b_1 for calculating the error in spectral index. I_1 is conservatively estimated at 2.0 mJy, and b_1 is estimated at 0.8 mJy.

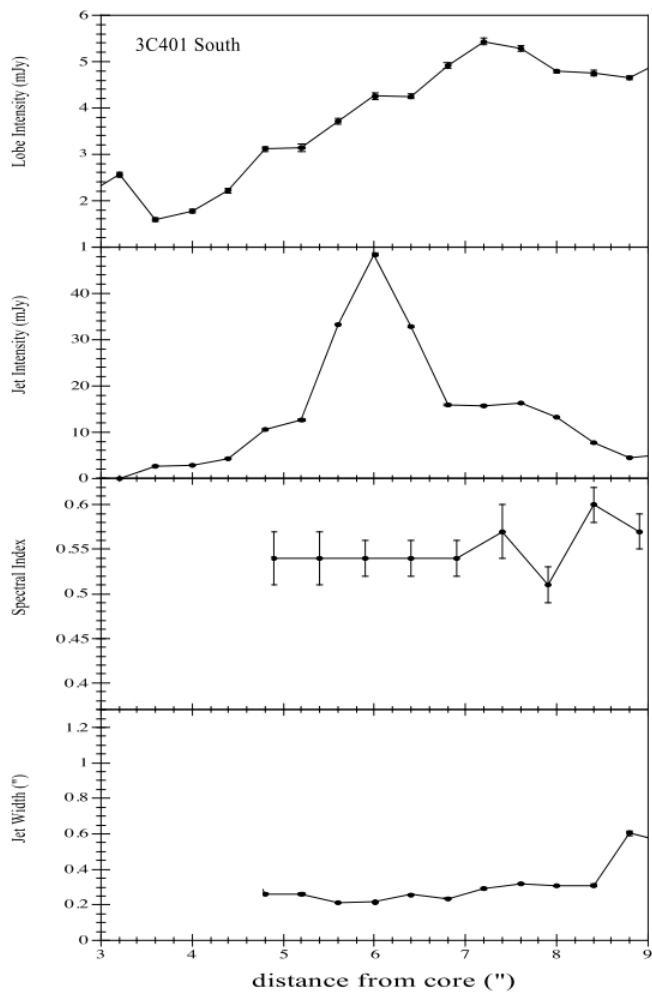


FIG. 14.—3C 401 South: distance vs. lobe intensity (top), jet intensity (top middle), spectral index of jet (bottom middle), and width of jet (bottom). The jet width is not corrected for the 0".25 beam at X band, so the first 7" are unresolved.

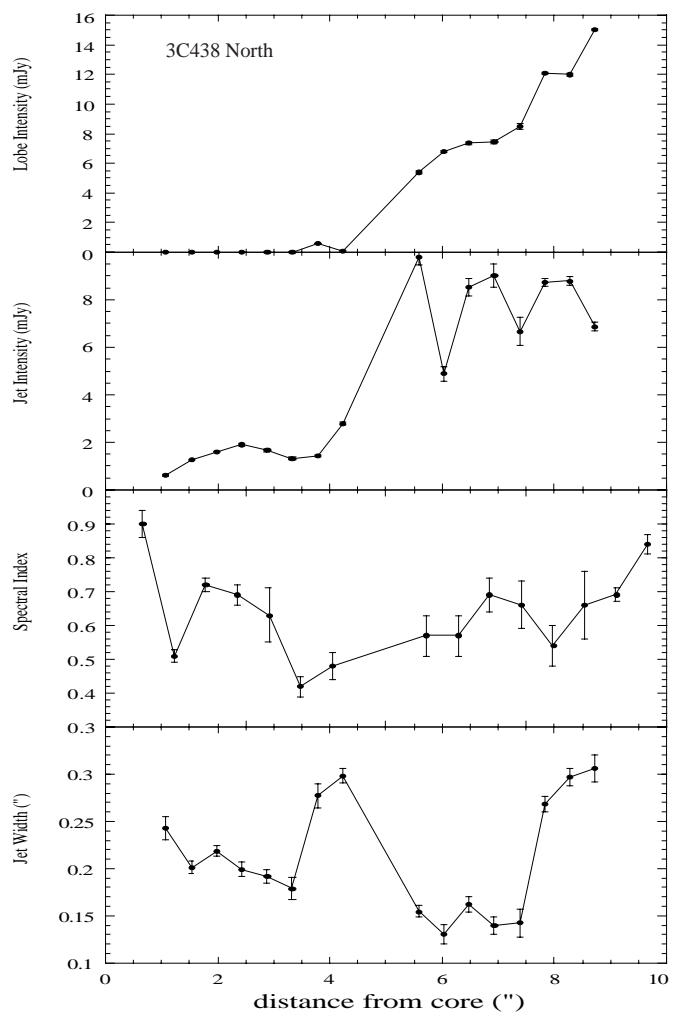


FIG. 15.—Same as Fig. 14, but for 3C 438 North

the graphs for the northern and southern jets of 3C 438, respectively. In the northern jet, the spectral index is flattest at approximately 3".5 from the core, with almost monotonic steepening in both directions. Just beyond the point at

which the spectrum flattens, there is a dramatic widening of the jet and an increase in the intensities of both the jet and the lobe. The steepest spectral indices in the southern jet are seen between 4" and 5" from the core. This steepening happens at the same point at which the jet narrows in

TABLE 2
JET CHANGE IN BRIGHTNESS UPON ENTERING LOBE

Source	Number of Jets	Change in Jet Brightness?	Reference
3C 28	1	Increase ^a	Leahy et al. 1997
3C 33.1	1	Increase ^b	Leahy et al. 1997
3C 200	1	No	Clarke, D. A., & Burns, J. O. (unpublished)
3C 219	1	Increase ^b	Clarke et al. 1992
3C 285	1	Increase	Leahy, Pooley, & Riley 1986
3C 288	2	Decrease	Bridle et al. 1989
3C 305	1	No	Leahy et al. 1997
3C 388	1	Increase ^b	Roettiger et al. 1994
3C 401	1	No	Hardcastle et al. 1997; Leahy et al. 1997
3C 438	2	Increase	Hardcastle et al. 1997; Leahy et al. 1997

^a The linear feature in the lobe, which is a straight extension from the jet, could be a filamentary feature such as the one seen in 3C 338 (Ge & Owen 1994), whose nature is still unclear.

^b Although lobe also shows a transition where the jet brightens, faint lobe material extends all the way back to the nucleus and becomes confused with lobe material from the opposite side.

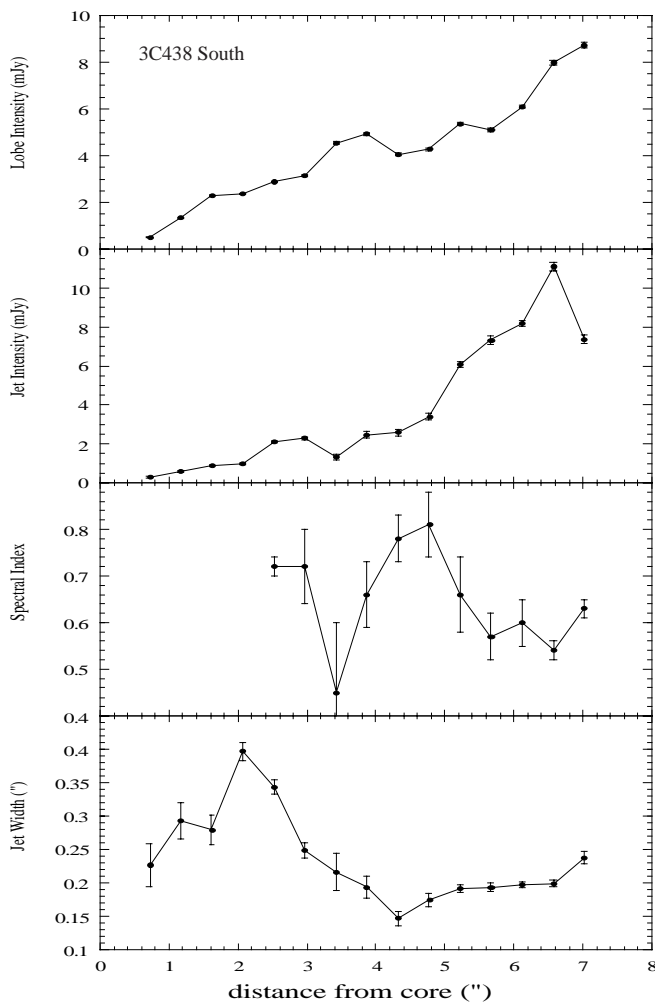


FIG. 16.—Same as Fig. 14, but for 3C 438 South

width—the opposite direction of the relation seen in the northern lobe.

3.6. Jet-Lobe Interactions

When looking at the intensities of the jet and lobe in the northern lobe of 3C 438 (Fig. 15), we found that, while the jet can be seen well before the lobe emission, it then brightens considerably as it enters the lobe. Seeing this effect in one source prompted us to look for similar examples in other sources. We used the DRAGN atlas (Leahy et al. 1997)⁴ to identify a sample of FR II radio galaxies with a jet and a lobe that did not remain bright all the way back to the core; i.e., there was a jet that “entered” the bright region of the lobe. Of the fifteen jets that met this criteria, twelve had cleanly separable jet and lobe emission, enabling further study.

Our sample of twelve jets (see Table 2) included nine that showed a significant change in jet brightness as they entered the bright lobe and three (3C 200, 3C 305, and 3C 401) that showed no significant change. In one source, 3C 288, the jet faded after it entered the lobe (see Fig. 17), while in the rest of the sources the jets brightened after entering the bright region of the lobe.

4. DISCUSSION

4.1. Mixed Spectral Indices

The basic model of FR II radio galaxies includes lobes whose spectra gradually steepen with distance from the hot spots because of aging of the emitting electrons. In the lobes of 3C 438, 3C 401, and 3C 153, the most diffuse parts of the emission follow this trend. However, we also see a complicated mixture of steep and flat spectral indices within the lobes. This mixture is seen in numerical simulations by Jones, Ryu, & Engel (1999). These simulations show that electrons may encounter a variety of shock types and strengths as they emerge from the jet, creating pockets of steep- and flat-spectrum electrons. This implies that these pockets of steep and flat spectra represent the *history* of particle acceleration of these electrons and do not necessarily reflect a *current site* of particle acceleration.

The C-shaped, flat-spectrum structure seen in the southern lobe of 3C 438 may also be a past termination point for a flapping jet. Such a jet has been suggested by Hardcastle et al. (1997) and is seen in numerical simulations (see, e.g., Norman 1996).

It is curious that our two best examples of mixed spectral indices, 3C 438 and 3C 401, are both in high-density environments. (They are found in clusters, are surrounded by faint, diffuse X-ray emission, and have unusually low polarization, indicating a dense magneto-ionic environment; Hardcastle et al. 1997). But is it also possible that the dense environment in some way caused the complicated spectral index structures that we see? Further comments about the interesting structures in these sources can be found in the DRAGN atlas.

The gradient in spectral index that we see in several of our sources is also seen in numerical simulations by Ryu & Jones (1999, private communication). In their simulations, the spectral index of the hot spots varied from 0.5 to 1.0 because of a strong magnetic field found at the end of the jet, which caused severe spectral steepening. The hot spots in our study had spectral indices that ranged from 0.68 to 1.28, but each individual hot spot only varied up to 0.2.

4.2. Structures Parallel to Jets

There are a growing number of structures seen parallel to jets, as we found in 3C 438. Other than their proximity and structural similarities to the jets, there is currently no way to separate these structures from random filamentary features in the lobes. Some parallel structures are seen in polarization (e.g., 3C 66B; Hardcastle et al. 1996; and 3C 219; Clarke et al. 1992), while others are seen in total intensity maps (e.g., Cygnus A; Katz-Stone & Rudnick 1994). For 3C 353 (Swain, Bridle, & Baum 1998), structures parallel to the jets are seen in both polarization and total intensity. These structures seen in FR I galaxies may also be related to the steep “cocoon” found around jets in WATs (Katz-Stone & Rudnick 1994; Katz-Stone et al. 1999). It is not clear how these various parallel structures are related to each other or to the particular example found in 3C 438.

One interpretation of these features is as a slower moving sheath surrounding a faster spine, or inner jet (Laing 1996). Spine/sheath models of jets have been shown to stabilize jets and may dominate jet dynamics (Sol, Pelletier, & Asséo 1989; Hanasz & Sol 1996). If the sheaths are slower moving, then at a given distance from the core the electrons in the sheath could have aged and steepened more if the magnetic

⁴ Available at <http://www.jb.man.ac.uk/atlas>.

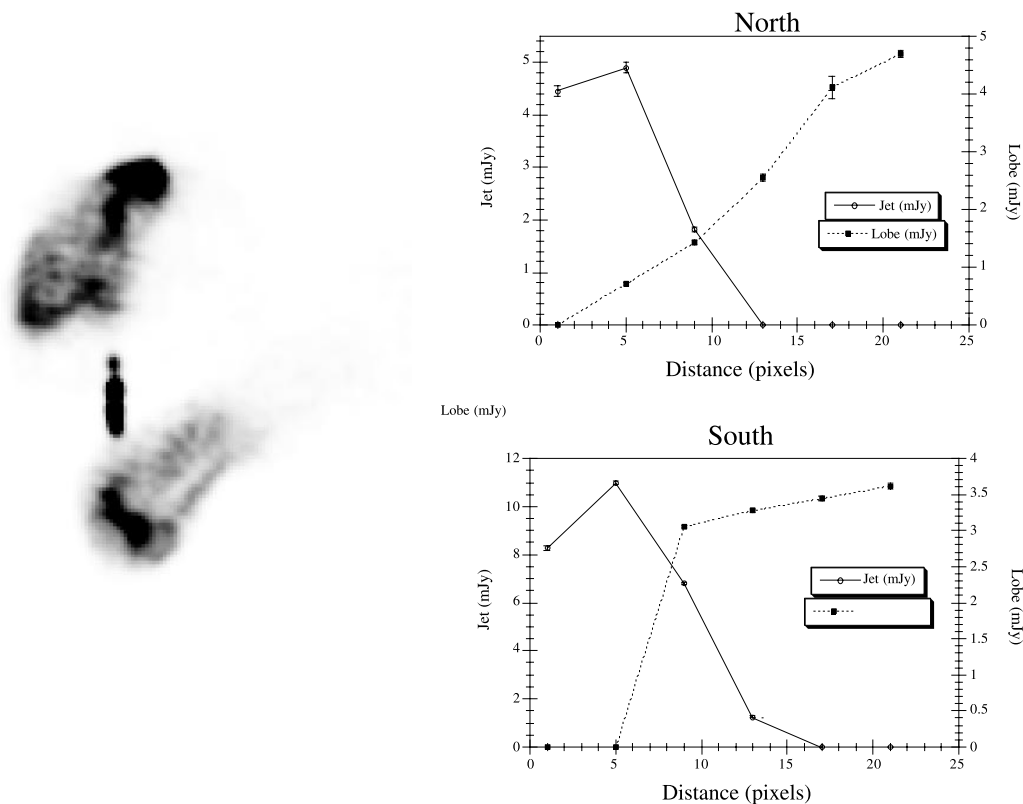


FIG. 17.—*Left*: Gray-scale image of 3C 288. *Right*: Intensity of jet and lobe for the north (*top*) and south (*bottom*) lobes.

fields in the jet and sheath are comparable. Alternatively, the same curved electron energy distribution could seem steeper in the sheath because of lower magnetic fields (Katz-Stone et al. 1999). While it may be possible that the parallel structure we see in 3C 438 is unrelated to the jet, this seems unlikely because of the close correspondence in their structure and brightness.

4.3. Spectra of Jets

The spectra of jets should reflect both the relativistic particle acceleration and loss histories. In WATs and other lower luminosity sources, the radio spectral index seems to be constant along the inner jet (3C 449, $\alpha = 0.53$; Katz-Stone & Rudnick 1997b; 3C 66B, $\alpha = 0.5$ to 0.6; Hardcastle et al. 1996; M87, $\alpha = 0.5$ to 0.6; Owen, Hardee, & Cornwell 1989). This suggests either that radiative losses are unimportant in the radio, or that the acceleration process is important all along the jet and robust to the physical variations causing brightness and width changes. Even the radio/optical spectral indices for 3C 66B (Jackson et al. 1993) or the derived power laws for M87 (Meisenheimer, Röser, & Schlötelburg 1996) show little variation along the jets. The strongest support for acceleration distributed along the jet comes from their X-ray detection (e.g., 3C 66B; Hardcastle, Birkinshaw, & Worrall 2001), for which the lifetime of the presumed synchrotron-emitting electrons can be as short as 30 yr.

Very little information exists on the spectra of FR II jets. 3C 236 shows considerable variation in the radio spectral index ($\alpha = 0.5$ to 1.5) of its inner components (Schillizzi et al. 2001). Cygnus A's jet shows a similarly steep spectrum and significant curvature up to 2 cm, with possible variation along the jet that is difficult to separate from the back-

ground (Katz-Stone, Rudnick, & Anderson 1993). As noted above, we find that 3C 401's jet has an approximately constant spectral index of $\alpha = 0.53$, similar to the FR I results above. We do see spectral variation in both jets of 3C 438, but these are not monotonic steepenings, as one might expect from simple radiative losses.

The origin of the spectral variations in the FR II jets is not clear. We looked for clues from the variations of spectrum, width, and intensity in 3C 438's jets. In the southern jet, we found that the spectral index steepens at the same point at which the jet narrows. In this same sense, in the northern jet the spectrum flattens as the jet widens. There are several possible explanations for this phenomenon, among which we are unable to distinguish at this time. One possibility is that there is no evolution of the particle spectrum along the jet, but that varying magnetic fields result in different local spectral indices. An arbitrary tuning of the relativistic electron densities would then be required to fit the local brightnesses. Another possibility is that particle acceleration occurs along the jet and varies with the local conditions. For example, the increase in jet width could be accompanied by increased jet turbulence, which could also increase particle acceleration, flatten the spectrum, and increase the intensity. A dramatic increase in intensity is seen immediately after the spectrum flattens at $\approx 3''.5$ from the core in the northern lobe of 3C 438. If there is particle acceleration at this point, multifrequency observations should show a power-law spectrum with a high break frequency.

We cannot draw conclusions from a single example, but the literature on FR II jets provides little additional guidance. Cygnus A's jet shows regions of expansion and constant width (Perley, Dreher, & Cowan 1984), although the connection to its knotty brightness profile is unclear. 3C 219

shows significant variations in jet width, which Bridle, Perley, & Henriksen (1986) suggest may be related to its local brightening. 3C 353 has a well-resolved jet width that remains virtually constant, although it has significant changes in brightness (Swain et al. 1998). Jet widths of four quasars are shown by Bridle et al. (1994) and have patterns of widening and narrowing similar to those seen here for 3C 438. These various behaviors and the different possible interpretations of 3C 438's behavior reflect very different physical pictures for the jet and the supply of relativistic particles to the hot spots and lobes. Sorting this out is likely to depend on multifrequency observations to measure local spectral shapes with sufficient resolution to separate knots from the underlying structure in the jets.

4.4. Jet-Lobe Interactions

As discussed above, in nine of the twelve cases where we could isolate the jet and lobe intensities, we found significant changes in these jets as they entered the bright part of the lobe. How does the lobe affect the jet? One possibility is that the turbulence in the lobe may disrupt the jet and cause it to lose its coherency; the jet will decrease in brightness, as seen in 3C 288. Or the lobe material may stimulate shocks in the jet (Jones et al. 1999), increasing its brightness, as we see for the majority of the sources we studied. Another possibility is that when the jet enters the lobe a second-order Fermi process reaccelerates particles in the boundary layer between the jet and lobe. If the increased brightness is caused by shocks stimulated by lobe material or by a second-order Fermi process in the boundary layer, the jet's spectrum should flatten as it enters the lobe. This flattening is a signature of particle acceleration. For the one jet in our study that enters the lobe and for which we have spectral index information (3C 438 North), we see a slight, but inconclusive, flattening of spectral index.

5. CONCLUDING REMARKS

The relevance of the simple cartoons of powerful radio galaxies has eroded over the years. The jets are not steady (see, e.g., Burns, Christiansen, & Hough 1982; Clarke & Burns 1991); indeed they may flap around near their terminus (Scheuer 1982), as indicated by both observations (Hardcastle et al. 1997) and numerical simulations (Hardee

& Norman 1990). As a consequence, the canonical steady terminal shock (Begelman, Blandford, & Rees 1974), at which relativistic particles can be accelerated, does not exist. This raises the question of where particle energy gains and losses actually occur in radio galaxies. This question is highlighted by recent optical and X-ray observations of jets (M87; Perlman et al. 1999; Pictor A; Wilson et al. 2001). Particle acceleration along the entire length of the jets may be required because of the short lifetimes of the radiating electrons. The nature of the broad but "jetlike" structure in Cygnus A's X-rays is unknown (Wilson et al. 2001). Instead of simple pictures of the backflowing cocoons, we see that backflows are not smooth, and lobes may be populated by filamentary features (Owen, Eilek, & Kassim 2000; Swain et al. 1998; Katz-Stone, Rudnick, & Anderson 1993). These may indicate flow instabilities, shocks, or turbulence from interaction with the jet and surrounding medium. In the weaker, FR I sources, there are clear indications of stratified jets or jet/sheath structures (Katz-Stone et al. 1999).

This new level of complexity is well illustrated in the latest generation of numerical simulations (Tregillis et al. 2001), which include relativistic particle acceleration, along with three-dimensional MHD. At issue is not simply the "weather" of radio galaxy structure, but the fundamental questions of what parts of the outgoing flow are actually visible as the "jet," how the unstable jet drives the overall source dynamics and structure, and where and how the bulk of the relativistic particle acceleration takes place.

The spectral tomography work presented here illustrates the type of information available and needed to address such issues. Further work using high-quality data is especially needed to follow up on (1) the spectral index structure in hot spot regions, (2) spectral index variations along jets, and (3) possible jet-lobe interactions. At the same time, broad explorations of parameter space with numerical simulations are needed to determine under what conditions behaviors like those reported here are found.

We would like to thank Robert Laing and Rick Perley for the use of their data. M. J. H. acknowledges support from PPARC grant GR/K98582. This work is partly supported at the University of Minnesota by grants AST 96-16964 and AST 00-71167 from the National Science Foundation.

REFERENCES

- Begelman, M. C., Blandford, R. D., & Rees, M. J. 1984, *Rev. Mod. Phys.*, 56, 255
 Bridle, A. H., Fomalont, E. B., Byrd, G. G., & Valtonen, M. J. 1989, *AJ*, 97, 674
 Bridle, A. H., Hough, D. H., Lonsdale, C. J., Burns, J. O., & Laing, R. A. 1994, *AJ*, 108, 766
 Bridle, A. H., Perley, R. A., & Henriksen, R. N. 1986, *AJ*, 92, 534
 Burns, J. O., Christiansen, W. A., & Hough, D. H. 1982, *ApJ*, 257, 538
 Celotti, A., Ghisellini, G., & Chiaberge, M. 2001, *MNRAS*, 321, L1
 Clarke, D. A., Bridle, A. H., Burns, J. O., Perley, R. A., & Norman, M. L. 1992, *ApJ*, 385, 173
 Clarke, D. A., & Burns, J. O. 1991, *ApJ*, 369, 308
 Cornwell, T. 1983, *A&A*, 121, 281
 Eilek, J. A., & Hughes, P. A. 1991, in *Beams and Jets in Astrophysics*, ed. P. A. Hughes (Cambridge: Cambridge Univ. Press), 428
 Ge, J., & Owen, F. N. 1994, *AJ*, 108, 1523
 Hanasz, M., & Sol, H. 1996, *A&A*, 315, 355
 Hardcastle, M. J., Alexander, P., Pooley, G. G., & Riley, J. M. 1996, *MNRAS*, 278, 273
 ———, 1997, *MNRAS*, 288, 859
 Hardcastle, M. J., Birkinshaw, M., & Worrall, D. M. 2001, *MNRAS*, 326, 1499
 Hardee, P. E., & Norman, M. L. 1990, *ApJ*, 365, 134
 Jackson, N., Sparks, W. B., Miley, G. K., & Macchetto, F. 1993, *A&A*, 269, 128
 Jones, T. W., Ryu, D., & Engel, A. 1999, *ApJ*, 512, 105
 Katz-Stone, D. M., & Rudnick, L. 1994, *ApJ*, 426, 116
 ———, 1997a, *ApJ*, 479, 258
 ———, 1997b, *ApJ*, 488, 146
 Katz-Stone, D. M., Rudnick, L., & Anderson, M. C. 1993, *ApJ*, 407, 549
 Katz-Stone, D. M., Rudnick, L., Butenhoff, C., & O'Donoghue, A. 1999, *ApJ*, 516, 716
 Laing, R. A. 1996 in *ASP Conf. Ser. 100, Energy Transport in Radio Galaxies and Quasars*, ed. P. E. Hardee, A. H. Bridle, & J. A. Zensus (San Francisco: ASP), 241
 Leahy, J. P. 1991 in *Beams and Jets in Astrophysics*, ed. P. A. Hughes (Cambridge: Cambridge Univ. Press), 100
 Leahy, J. P., Bridle, A. H., & Strom, R. G. 1997, *An Atlas of DRAGNs* (Manchester: Jodrell Bank Obs.)
 Leahy, J. P., & Perley, R. A. 1991, *AJ*, 102, 537
 Leahy, J. P., Pooley, G. G., & Riley, J. M. 1986, *MNRAS*, 222, 753
 Meisenheimer, K., Röser, H.-J., & Schlötelburg, M. 1996, *A&A*, 307, 61
 Norman, M. L. 1996 in *ASP Conf. Ser. 100, Energy Transport in Radio Galaxies and Quasars*, ed. P. E. Hardee, A. H. Bridle, & J. A. Zensus (San Francisco: ASP), 319
 Owen, F. N., Eilek, J. A., & Kassim, N. E. 2000, *ApJ*, 543, 611
 Owen, F. N., Hardee, P. E., & Cornwell, T. J. 1989, *ApJ*, 340, 698
 Perley, R. A., Dreher, J. W., & Cowan, J. J. 1984, *ApJ*, 285, L35
 Perlman, E. S., Biretta, J. A., Zhou, F., Sparks, W. B., & Macchetto, F. D. 1999, *AJ*, 117, 2185

- Roettiger, K., Burns, J. O., Clarke, D. A., & Christiansen, W. A. 1994, *ApJ*, 421, L23
- Rudnick, L. 2001a, in *ASP Conf. Ser.*, *Particles and Fields in Radio Galaxies*, ed. R. A. Laing & K. M. Blundell, in press
- , 2001b, *ApJ*, submitted
- Rudnick, L., & Katz-Stone, D. M. 1996, in *ASP Conf. Ser.* 100, *Energy Transport in Radio Galaxies and Quasars*, ed. P. E. Hardee, A. H. Bridle, & J. A. Zensus (San Francisco: ASP), 233
- Rudnick, L., Katz-Stone, D. M., & Anderson, M. C. 1994, *ApJS*, 90, 955
- Scheuer, P. A. G. 1982, in *IAU Symp.* 97, *Extragalactic Radio Sources*, ed. D. S. Heeschen & C. M. Wade (Dordrecht: Reidel), 163
- Schilizzi, R. T., et al. 2001, *A&A*, 368, 398
- Sol, H., Pelletier, G., & Asséo, E. 1989, *MNRAS*, 237, 411
- Swain, M. R., Bridle, A. H., & Baum, S. A. 1998, *ApJ*, 507, L29
- Tregillis, I., Jones, T. W., & Ryu, D., 2001, *ApJ*, 557, 475
- Wilson, A., Young, A. J., & Shopbell, P. L. 2001, in *ASP Conf. Ser.*, *Particles and Fields in Radio Galaxies*, ed. R. A. Laing & K. M. Blundell, in press (preprint astro-ph/0101422)